Journal of Power Sources 195 (2010) 4971–4976

Contents lists available at ScienceDirect

Journal of Power Sources

journal homepage: www.elsevier.com/locate/jpowsour

Factors affecting Li mobility in spinel $LiMn_2O_4$—A first-principles study by GGA and GGA+*U* methods

Bo Xu [a], Shirley Meng [a,b,*]

[a] *Department of NanoEngineering, University of California San Diego, 9500 Gilman Drive, La Jolla, CA 92093, United States*
[b] *Department of Materials Science and Engineering, University of Florida, 100 Rhines Hall, Gainesville, FL 32611, United States*

ARTICLE INFO

Article history:
Received 12 January 2010
Received in revised form 20 February 2010
Accepted 22 February 2010
Available online 26 February 2010

Keywords:
Spinel
First-principles calculation
Lithium mobility

ABSTRACT

The structural changes and voltages of $LiMn_2O_4$ spinel as a function of lithium content were investigated with density functional theory (DFT) in the generalized gradient approximation (GGA) and in the GGA with Hubbard *U* correction (GGA+*U*). The GGA+*U* approximation can distinguish the charge separation between Mn^{3+} and Mn^{4+}, which GGA fails to capture. Therefore with this method the effects of local environments on Li diffusion activation energy barriers in the Li-rich phase could be systematically investigated. Our results showed that the different valences states of Mn ions and their arrangement surrounding the lithium ions have a profound effect on the activation barrier of lithium diffusion in the spinel structure.

1. Introduction

$LiMn_2O_4$ spinel and its derivatives are presently the center of much interest as the cathodes of high-power lithium batteries for transportation applications. The commercialization of the material has been long delayed by the self-discharge problem when left under fully charged, particularly at elevated temperatures; however, this obstacle may be lifted by chemical stabilization with aluminum doping, as well as modifying the salt in electrolyte [1–4].

In principle, it is believed that the spinel phase, whose cubic structure ensures three-dimensional diffusion paths, can deliver high power even though the theoretical capacity of the $LiMn_2O_4$ is only approximately 140 mAh g^{-1} in the voltage range of 3.0–4.3 V. However, the stoichiometric $LiMn_2O_4$ is found to have inferior rate capability. The volume change between the fully delithiated material and the pristine material is about 7% [5,6]. When the material is charged/discharged at room temperature, two voltage plateaus appear at around 4.1 V and 4.0 V (vs. Li). The two voltage steps are attributed to the order–disorder transition of the Li^+-vacancy arrangement when the Li concentration is around 50% [5,7,8]. A number of theoretical/computational investigations have been performed on this material [9–12]. A phase diagram of the $Li_xMn_2O_4$ has been calculated using local density approximation (LDA) to the density functional theory (DFT) [12]. Though in this former study [12] it can successfully explain the phase transformation when x varies from 1 to 2 (cubic to tetragonal phase transformation), the phase stability, lattice change and voltage are not consistent with the experimental observations when x varies in the range of 0–1. The main reason can be attributed to the fact, that neither the LDA nor the GGA approach can give the distinguished electronic structures of Mn^{3+}/Mn^{4+} ions in $LiMn_2O_4$, which is experimentally observed with neutron diffraction (ND) and magnetic studies [13,14]. When referring to the kinetic properties, molecular dynamics (MD) simulations and dynamic Monte Carlo simulations have been used to investigate the Li diffusivities in the material [9,11]. Most of the studies focus on the temperature dependence and Li concentration dependence on the Li diffusivities without considering the valence changes in transition metal ions. It is well known that the change of Li concentration leads to the valence change of the transition metal (Mn) ions. Such change might have a strong effect on the Li mobility in an ionic crystal since lithium diffusion occurs through a thermally activated state surrounded by transition metal ions (more details given in Section 3). It is also experimentally observed that certain doping elements (e.g. Ni) gives remarkable rate capability compared with undoped $LiMn_2O_4$ [15–17].

The Hubbard *U* value in the Hamiltonian, needed to correct for the self-interaction error on transition metal oxides in DFT, is implemented in this work. There have been ample evidences showing that the GGA+*U* method can give more accurate voltage predictions in transition metal oxides [18,19]. In GGA method, charges are spuriously delocalized: for example, in $LiMn_2O_4$, all Mn ions show an average valence of 3.5^+. On the other hand, GGA+*U* method gives half Mn^{3+} and half Mn^{4+}, which more accurately capture the physics in the actual material.

* Corresponding author at: Department of NanoEngineering, University of California San Diego, 9500 Gilman Drive, La Jolla, CA 92093, United States.
E-mail address: shirleymeng@ucsd.edu (S. Meng).

0378-7753/$ – see front matter
doi:10.1016/j.jpowsour.2010.02.060

By comparing the results obtained from GGA and GGA+*U* methods, we found that the redox potentials of $LiMn_2O_4$ and the trend of lattice parameter change as a function of lithium content can be more accurately calculated with the GGA+*U* method. More importantly, it is clearly demonstrated in our study that different valence states of Mn ions and their arrangements surrounding the lithium ions have a profound effect on the activation barrier of lithium diffusion in the spinel structure.

2. Computation method

In this work, a supercell composed of eight-formula units of $Li_xMn_2O_4$ is used. Calculations were performed in the spin-polarized GGA and GGA+*U* approximations to the DFT. Core electron states were represented by the projector augmented-wave method [20] as implemented in the Vienna ab initio simulation package (VASP) [21–23]. The Perdew Burke Ernzerhof exchange correlation [24] and a plane wave representation for the wavefunction with a cutoff energy of 400 eV were used. The Brillouin zone was sampled with a mesh by Monkhorst packing. The atomic positions and cell parameters are fully relaxed to obtain total energy and optimized cell structure. To obtain the accurate electronic density of states (DOS), a static self-consistent calculation is run, followed by a non-self-consistent calculation using the calculated charge densities from the first step. The cell volume is fixed with internal relaxation of the ions in the second step calculation. A supercell with one vacancy out of eight Li sites ($Li_7Mn_{16}O_{32}$) is used to calculate the Li diffusion activation barriers in Li-rich phase. The Hubbard *U* correction is introduced to describe the effect of localized *d* electrons of Mn ions. Previous work has shown that the *U* values can be calculated in a self-consistently way [25]. In spinel structure, the *U* value of Mn^{3+} ions is 4.64 while the *U* value of Mn^{4+} ions is 5.04 [18]. Because in $LiMn_2O_4$, Mn^{3+} and Mn^{4+} ions co-exist, a unique effective *U* value of 4.84 is applied in rotationally invariant LSDA+*U* approach [26]. Test calculations have been performed to assign distinguished effective *U* values to Mn^{3+} and Mn^{4+} ions in the same supercell, and similar Mn valence separation can be observed.

3. Results and discussion

3.1. Voltage and lattice parameters correction

In manganese spinel, phase separations happen while Li ions are intercalating into and de-intercalating from the cathode materials. Rather than forming a solid solution $Li_xMn_2O_4$ ($0 < x < 1$), experimental studies [5,27–29] have shown voltage plateaus around 4.0 V and 4.1 V appears during the charge/discharge processes. There is a small voltage step at $x = 0.5$ as the result of a stable Li-vacancy ordered phase. Voltage plateaus appear when there is two phases co-exist at certain Li concentration ranges.

For any intercalation system, the total Gibbs free energy can be written as:

$$dG = -S\,dT + V\,dP + \sum_i \mu_i N_i$$

where *S* is the entropy, *T* is the temperature, *V* is the volume, *P* is the pressure, μ_i is the chemical potential of element *i* and N_i is the amount of element *i*. All the elements except Li are treated as the host of the intercalation electrode materials (M) and their chemical potentials do not change during the charge/discharge process. Therefore the Gibbs free energy can be rewritten as:

$$dG = -S\,dT + V\,dP + \mu_{\mathrm{Li}}\,dN_{\mathrm{Li}} + \mu_{\mathrm{M}}\,dN_{\mathrm{M}}$$

When the temperature and pressure of the system are kept constant, the equation can be simplified to $dG = \mu_{\mathrm{Li}} dN_{\mathrm{Li}}$. Therefore the chemical potential of Li ions can be calculated as $\mu_{\mathrm{Li}} = dG/dN_{\mathrm{Li}}$. From Nernst equation, the voltage of the cell can be expressed as

$$\text{voltage} = -\frac{\mu_{\mathrm{Li}}^{\mathrm{cathode}} - \mu_{\mathrm{Li}}^{\mathrm{anode}}}{ze}$$

where $\mu_{\mathrm{Li}}^{\mathrm{cathode}}$ is the chemical potential per atom of Li in the cathode and can be calculated from above equations, $\mu_{\mathrm{Li}}^{\mathrm{anode}}$ is the chemical potential per atom of Li in the anode. *z* is the valence of the ion. For Li ions, *z* equals to 1. And *e* is the absolute value of the electron charge.

In our study, the total energy *G* of the eight-formula supercell with different Li concentrations $LiXMn_{16}O_{32}$ are obtained from first-principles calculations performed at zero Kelvin. Their formation enthalpies can be calculated and plotted as a function of Li concentration to obtain the formulas of stable phases (results not shown here). When GGA method is applied, $LiXMn_{16}O_{32}$ is stable for each *X* from 1 to 7, suggesting a solid solution behavior which is contrary to experimental observations. In this case, the chemical potential of Li ions in cathode at each *X* can be approximated by:

$$\mu_{\mathrm{Li}}^{\mathrm{LiXMn_{16}O_{32}}} = \frac{dG}{dN_{\mathrm{Li}}} \approx G_{\mathrm{LiX+1Mn_{16}O_{32}}} - G_{\mathrm{LiXMn_{16}O_{32}}} \quad (0 \le X \le 8)$$

When GGA+*U* is applied, only one stable intermediate phase is found at $X = 4$, suggesting that phase separations happen in two stages, $0 \le X \le 4$ and $4 \le X \le 8$. In each stage, the chemical potentials of Li ions in both phases are equal, therefore can be approximated by:

$$\mu_{\mathrm{Li}}^{\mathrm{LiXMn_{16}O_{32}}} = \frac{G_{\mathrm{Li_4Mn_{16}O_{32}}} - G_{\mathrm{LiMn_{16}O_{32}}}}{4-0} \quad (X = 0, 4)$$

and

$$\mu_{\mathrm{Li}}^{\mathrm{LiXMn_{16}O_{32}}} = \frac{G_{\mathrm{Li_8Mn_{16}O_{32}}} - G_{\mathrm{Li_4Mn_{16}O_{32}}}}{8-4} \quad (X = 4, 8)$$

Li metal is used as the reference anode materials, and the calculated Li chemical potential in Li metal is $\mu_{\mathrm{Li}}^{\mathrm{anode}} = -1.9\,\mathrm{eV}$. The voltage profiles calculated by both GGA and GGA+*U* approaches are plotted in Fig. 1(i). The average voltage over all Li concentrations is 3.4 V calculated by GGA, which underestimates the voltage by 17.0% when comparing to the experimental value. The step-wise calculated voltage profile is due to the fact that only average voltages of lithium concentration intervals are computed. With GGA+*U* methods, the two voltage plateaus are shown at 4.02 V and 4.04 V due to the presence of one (and only) intermediate stable phase at $Li_{0.5}Mn_2O_4$. Not only the calculated average voltage is with 1% difference from the experimental value, but also the two-phase separations are accurately captured by GGA+*U* method. The absolute value of the voltage step (20 meV) calculated with GGA+*U* is smaller than the 100 meV observed value. This may be due to the coupling effect of Li/vacancy ordering and Mn^{3+}/Mn^{4+} ordering in $Li_{0.5}Mn_2O_4$. More vigorous study is underway to explore this complex phenomenon.

Fig. 1(ii) shows the lattice parameters of the $Li_xMn_2O_4$ cubic unit cell as a function of Li concentration. At $x = 1$, GGA+*U* method overestimates the lattice parameter comparing to the experimental observation by 2%, while the absolute value of GGA calculation is closer to the experimental value. However, the total observed volume change from $LiMn_2O_4$ to Mn_2O_4 is around 6–7% in experiments. Using GGA+*U* method, the volume change from $LiMn_2O_4$ to Mn_2O_4 is calculated as 6.3%, while using GGA method, the volume change from $LiMn_2O_4$ to Mn_2O_4 is only 0.7%. Two sets of experimental data are used for this comparison [5,6] and the inconsistence in absolute experimental

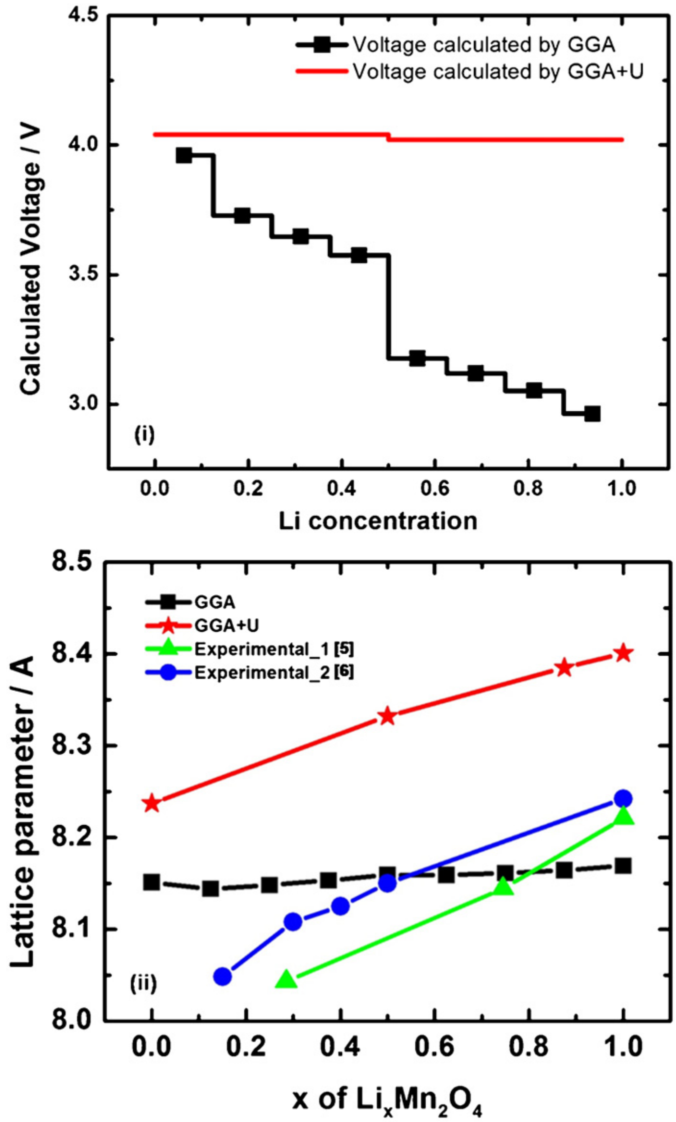

Fig. 1. (i) Voltage calculated by GGA and GGA+U methods; (ii) calculated and experimentally measured lattice parameters of the $Li_xMn_2O_4$ cubic unit cell as a function of Li concentration.

values is the result of different precursors and synthesis conditions.

The Jahn-Teller distortion of individual Mn^{3+} ions can be observed by the lattice parameter change using GGA+U method. In $LiMn_2O_4$ materials, each Mn ion is surrounded by an octahedron formed by six oxygen ions. The Mn–O bonds are formed with the hybridization between O *2p* orbitals and Mn *3d* orbitals. As described in ligand field theory [30], the octahedral crystal field splits the Mn *3d* orbitals to two types of orbitals, t_{2g} orbitals with lower energy level and e_g orbitals with higher energy level. When there is a single un-paired electron in e_g orbitals, as in Mn^{3+} ions, the Mn–O bond pointing towards vertex O will be elongated or contracted due to the asymmetric shape of *d* electron clouds. The effect is well known as the Jahn-Teller distortion [31]. In Mn_2O_4 structure, no Mn^{3+} exists and the lattice remains perfect cubic in GGA+U calculations. However, in $LiMn_2O_4$ structure, half of the Mn ions are Mn^{3+}, which leads to the remarkable effect of Jahn-Teller distortion and the Mn^{3+}–O bondlengths split, subsequently the structure changes from cubic to tetragonal when lithium concentration $x = 1$. Such cubic to tetragonal phase transformations have been observed in $LiMn_2O_4$ at temperatures below 100 K [32–34]. In GGA method,

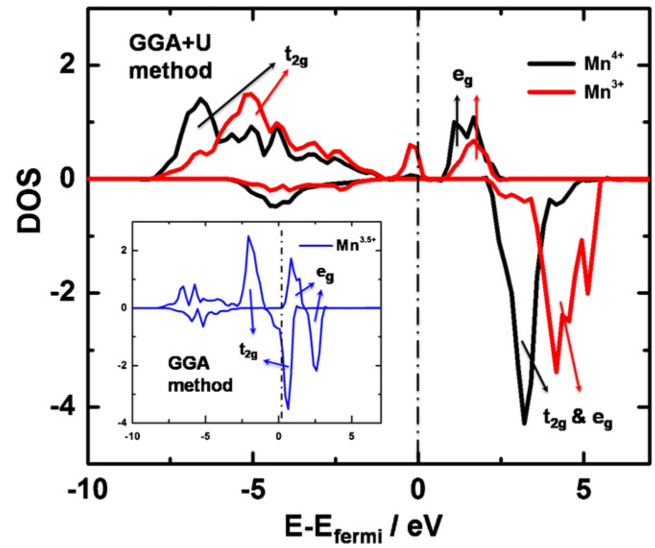

Fig. 2. Mn *3d* electron density of state (DOS) plots using GGA+U and GGA (insert) methods.

both Mn_2O_4 and $LiMn_2O_4$ structure maintains cubic structure at zero Kelvin.

3.2. Electronic structure of Mn^{3+} and Mn^{4+}

The electron configuration of Mn^{3+} ion is $t_{2g}{}^3e_g{}^1$ and Mn^{4+} ion is $t_{2g}{}^3$. The two ions can be distinguished clearly from the differences in DOS calculated using GGA+U method (Fig. 2). In the projected Mn^{4+} DOS (black), the energy levels of t_{2g} orbitals with spin-up states are lower than the Fermi energy level, indicating that the spin-up states in t_{2g} orbitals are fully occupied. The energy levels of t_{2g} orbitals with spin-down states and the entire e_g orbitals energy levels are above the Fermi energy. These orbitals are unoccupied. The DOS plot is consistent with the $t_{2g}{}^3$ electron configuration of Mn^{4+} ion. In the projected Mn^{3+} DOS (red), the spin-up states of e_g orbitals split to two peaks. The energy level of one peak is lower than Fermi energy indicating that one of the e_g orbitals is occupied, which is consistent with the $t_{2g}{}^3e_g{}^1$ electron configuration of Mn^{3+} ion.

The DOS plot calculated using GGA method is also given as an insert in Fig. 2 for comparison. Only one type of DOS (blue) can be obtained for all Mn ions in the supercell. The spin-up states and half of the spin-down states of t_{2g} orbitals are occupied, indicating an average valence of +3.5 for each Mn ion.

3.3. The effect of Mn charge distribution on Li diffusion activation barrier

To understand how the Mn charge distribution will affect the lithium diffusion, we have to look at the atomic arrangement of the spinel $Li_xMn_2O_4$ structure. Fig. 3(i) illustrates the structure of $LiMn_2O_4$. The spinel $LiMn_2O_4$ belongs to $Fd\bar{3}m$ space group with oxygen ions in *32e* sites forming a close-packed *fcc* lattice. Mn ions reside on the *16d* octahedral sites, while the Li ions sit in the *8a* tetrahedral sites. The *16c* octahedral sites are left empty. The Li ions diffusion occurs by hopping from one *8a* site to another *8a* site through the intermediate *16c* site (Fig. 3(ii)). Because each face of *8a* site is shared with a *16c* site, three-dimensional diffusion paths can be formed inside the structure (Fig. 3(iii)). Each *16c* site is surrounded by six Mn ions forming a Mn ring in the plane that is perpendicular to the Li diffusion paths (Fig. 3(iv)). The total energy of the supercell varies with the migration path of the mobile Li ion

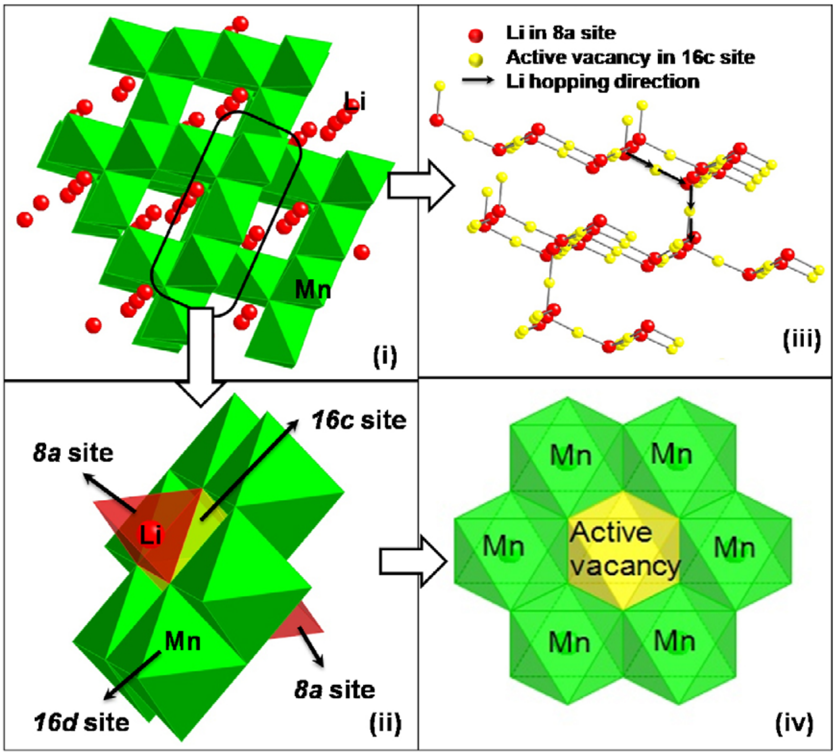

Fig. 3. Three-dimensional lithium diffusion paths in $LiMn_2O_4$.

and a maximum value is achieved when the Li ions are in the *16c* sites. The energy difference between Li in the initial state (*8a*) and in metastable state (*16c*) is considered as the Li diffusion activation barrier E_a [9]. In this work, different valence configurations in the local Mn rings are implemented using GGA+*U* method, and their effect on Li diffusion activation barriers are investigated.

In each Mn ring, the number of Mn^{4+} ions N_{IV} can vary from 0 to 6. However, when $N_{IV} = 6$ or 0, the structure are energetic unfavorable because they will introduce high charge localization and result in strong coulombic interactions inside the structure. In our study, the value of N_{IV} is limited to $1 \leq N_{IV} \leq 5$. For each value of N_{IV}, different Mn^{3+}–Mn^{4+} arrangements can be found and each of them is treated as a distinct configuration. A total number of seven configurations are investigated. They are listed in Table 1 and labeled by characters from "a" to "g". For each configuration, the corresponding Li diffusion activation barriers are calculated.

The calculations are performed in a Li-rich phase supercell ($Li_7Mn_{16}O_{32}$). The variations of Li diffusion barriers versus the number of Mn^{4+} ions in the Mn rings are depicted in Fig. 4(i). When Li ions are in the *16c* site, the *16c* site octahedral volumes and distances of the mobile Li to its nearest Mn ions are also analyzed. The results are presented in Fig. 4(ii) and (iii), respectively. The seven configurations can be sorted to three categories by different ranges of Li diffusion activation barriers: (separated by dash lines in Fig. 4(i)), (1) Low barrier case ($E_a < 400$ meV); (2) Medium barrier case; (3) High barrier cases ($E_a < 750$ meV).

(1) In low barrier case, there are more Mn^{4+} ions than Mn^{3+} ions in the Mn ring, suggesting that Li ions are more favored to be surrounded by Mn^{4+} ions. The reason can be attributed to the electrostatic effect. As there are three types of cations in $LiMn_2O_4$, Li^+ ions, Mn^{3+} ions and Mn^{4+} ions, the combination of Li^+ ions and Mn^{4+} ions can minimize the positive charge localization and further reduce the total energy of the system. Comparing to Mn^{3+} ions, the electron clouds of Mn^{4+} ions are less dense, causing weaker Mn–O interaction and longer Mn–O bondlength. Consequently, the Li–O bondlength is shortened, leading to smaller Li *16c* site octahedral volumes (Fig. 4(ii)a–c). On the other hand, the Li^+–Mn^{4+} distances are longer than Li^+–Mn^{3+} distances due to the stronger coulombic

Table 1
Mn valence configurations in Mn-rings surrounding the diffusing Li^+ in the activated site.

	# of Mn^{4+}	Label	Mn1	Mn2	Mn3	Mn4	Mn5	Mn6
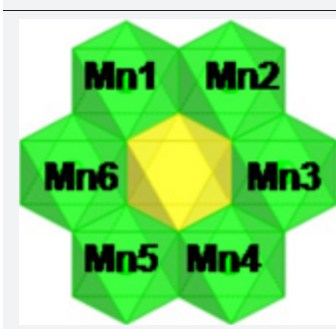	5	a	4+	4+	4+	4+	4+	3+
	4	b	4+	4+	3+	4+	4+	3+
		c	4+	4+	4+	3+	4+	3+
	3	d	4+	3+	4+	3+	4+	3+
		e	4+	4+	3+	4+	3+	3+
	2	f	4+	3+	3+	4+	3+	3+
	1	g	4+	3+	3+	3+	3+	3+

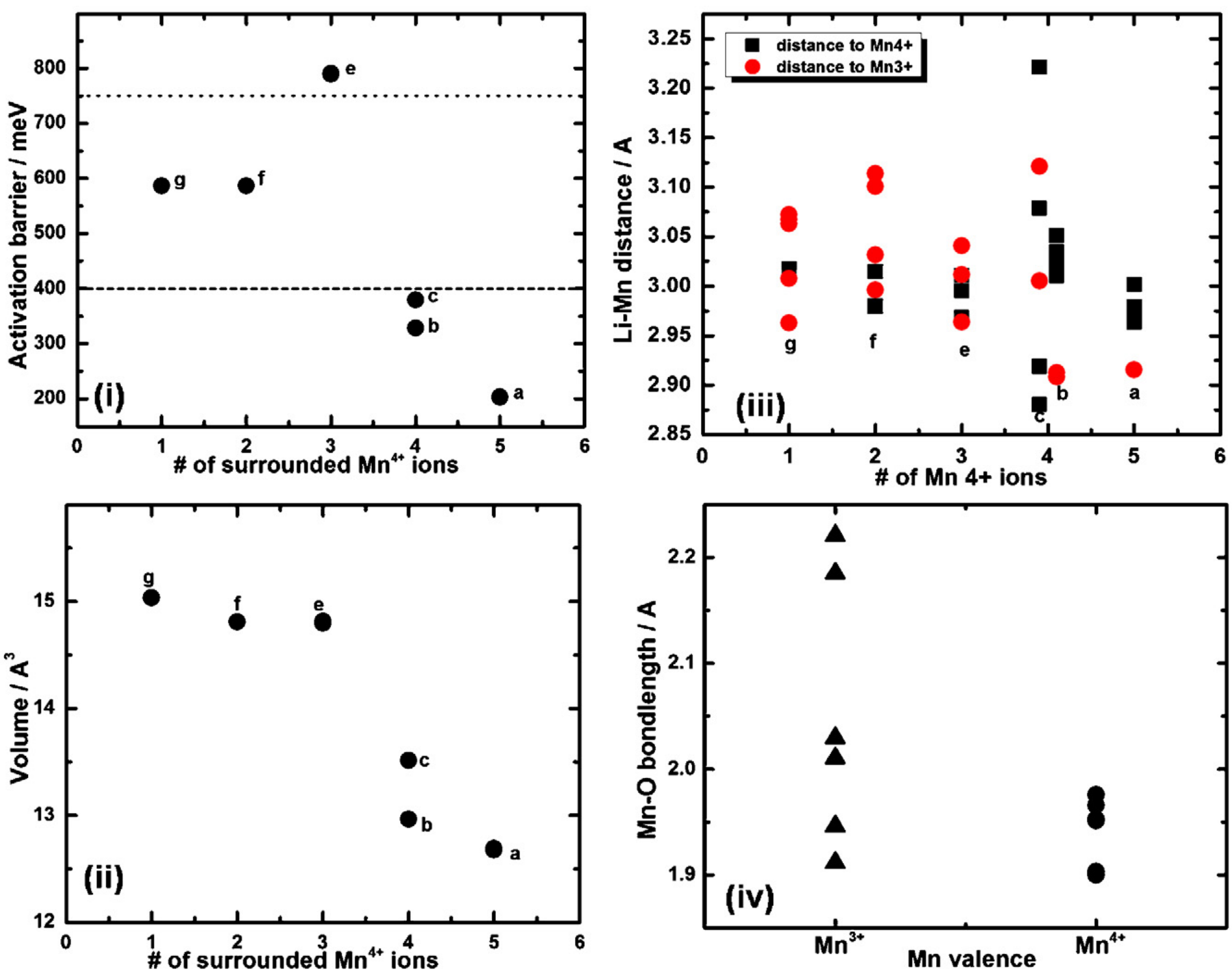

Fig. 4. (i) Local environment dependent Li diffusion activation barriers in $Li_7Mn_{16}O_{32}$; (ii) active Li *16c* site octahedral volumes; (iii) distances between the mobile Li ion and surrounding Mn ions; (iv) Mn–O bondlengths of Mn^{3+}/Mn^{4+} in configuration e.

repulsion between Li^+ and Mn^{4+} than Li^+ and Mn^{3+}, as shown in Fig. 4(iii) for configurations a and b "Li-Mn bondlengths" split. For configuration c, the different trend may be attributed to the asymmetric Mn^{3+}/Mn^{4+} distribution in the ring. When Li is closer to some Mn^{3+} ions, it is also closer to another Mn^{4+} ion, therefore when the electrostatic balance is reached, the Li–Mn^{3+}/Mn^{4+} distances spread with wide distribution.

(2) In medium barrier case, the number of Mn^{4+} ions is smaller than Mn^{3+} ions. There is one more electron in Mn^{3+} ion than in Mn^{4+} ion and the hybridization between O *2p* electrons and Mn *3d* electrons are stronger. The Mn–O bondlengths are shortened, leaving more space for the Li *16c* site (Fig. 4(ii)f and g). The total screening effect of the electron clouds between Li ions and Mn ions are strengthened, as a result, the "Li–Mn bondlength" split disappears (Fig. 4(iii)f and g).

(3) In high barrier case, the numbers of Mn^{4+} ion and Mn^{3+} ion are equal. In configuration d, Li cannot be stabilized in *16c* site, indicating that lithium diffusion through this type of activated site is energetically unfavorable. The specific high energy barrier of configuration e might be attributed to the local Jahn-Teller effect of Mn^{3+}. As mentioned in section 3.1, the Jahn-Teller effect will elongate or contract the Mn *16d* octahedron along the axis pointing to the vertex O ions. Fig. 4(iv) presents the Mn–O bondlength for a Mn^{3+} ion and a Mn^{4+} ion. The two Mn ions are from the Mn rings with configuration e, but the trend is consistent in all configurations. The Mn–O bondlengths of a Mn^{4+} ion are almost the same while there is a bondlength split for the Mn^{3+} ion. Therefore, the Mn^{3+} octahedron is highly distorted and the positions of their O ions are displaced from their ideal positions. In the Mn rings, adjacent Mn octahedrons share two oxygen ions as vertex, therefore, if a Mn^{3+} is adjacent to a Mn^{4+}, the octahedron edge-misfit will be introduced, leading to high internal strains. When the number of Mn^{4+} ion and Mn^{3+} ion is equal, many Mn^{3+}–Mn^{4+} adjacencies are created. These internal strains might cause the diffusing Li ions less stable and elevate the diffusion barriers.

Our results reveal that a larger amount of Mn^{4+} ions may enhance the ionic conductivity by lowering local Li diffusion activation barriers. We speculate this could be one of the main contributing factors for the improved rate capability in Ni, Co or Cu doped manganese spinel materials [15,35,36], since these doping elements are in 2+ and push more Mn ions to 4+.

4. Conclusion

For volume changes and lithium intercalation voltages, the results obtained from GGA+*U* method are qualitatively more accurate than those obtained by GGA method. The Mn^{3+} and Mn^{4+} ions can be distinguished by introducing the Hubbard *U* correction in the DFT. Surprisingly, the higher amount of Mn^{4+} ions enhances the ionic conductivity by making local Li diffusion activation barriers lower. Our study clearly shows the necessity in correcting self-interaction in localized electron systems, such as $LiMn_2O_4$. More importantly, the results shed some light on understanding the role of local charge distribution on the lithium diffusion activation barrier of the $LiMn_2O_4$ spinel materials.

Acknowledgements

This material is based upon work supported as part of the Northeastern Center for Chemical Energy Storage (NECCES), an Energy Frontier Research Center funded by the U.S. Department of Energy, Office of Science, Office of Basic Energy Sciences under Award Number DE-SC 0001294 (subcontract to UCSD 51055). Computing resources are provided by UCSD Triton Resource at San Deigo Supercomputer Center and University of Florida High Performance Computing Center. Y.S. Meng gratefully acknowledges support from the new faculty startup funds from UCSD and UF.

References

[1] R.J. Gummow, A. Dekock, M.M. Thackeray, Solid State Ionics 69 (1994) 59–67.
[2] A. Eftekhari, Solid State Ionics 167 (2004) 237–242.
[3] Y.J. Shin, A. Manthiram, J. Electrochem. Soc. 151 (2004) A204–A208.
[4] Z.H. Chen, W.Q. Lu, J. Liu, K. Amine, Electrochim. Acta 51 (2006) 3322–3326.
[5] H. Berg, J.O. Thomas, Solid State Ionics 126 (1999) 227–234.
[6] K. Kanamura, H. Naito, T. Yao, Z. Takehara, J. Mater. Chem. 6 (1996) 33–36.
[7] H. Abiko, M. Hibino, T. Kudo, Electrochem. Solid State 1 (1998) 114–116.
[8] J.S. Kim, J. Prakash, J.R. Selman, Electrochem. Solid State 4 (2001) A141–A144.
[9] R. Darling, J. Newman, J. Electrochem. Soc. 146 (1999) 3765–3772.
[10] I.Y. Gotlib, I.V. Murin, E.M. Piotrovskaya, Inorg. Mater. 39 (2003) 404–408.
[11] C.Y. Ouyang, S.Q. Shi, Z.X. Wang, X.J. Huang, L.Q. Chen, Solid State Commun. 130 (2004) 501–506.
[12] A. Van der Ven, C. Marianetti, D. Morgan, G. Ceder, Solid State Ionics 135 (2000) 21–32.
[13] S.K. Mishra, G. Ceder, Phys. Rev. B 59 (1999) 6120–6130.
[14] V. Massarotti, D. Capsoni, M. Bini, G. Chiodelli, C.B. Azzoni, M.C. Mozzati, A. Paleari, J. Solid State Chem. 131 (1997) 94–100.
[15] H. Xia, Y.S. Meng, L. Lu, G. Ceder, J. Electrochem. Soc. 154 (2007) A737–A743.
[16] K.M. Shaju, P.G. Bruce, Dalton Trans. (2008) 5471–5475.
[17] M. Kunduraci, J.F. Al-Sharab, G.G. Amatucci, Chem. Mater. 18 (2006) 3585–3592.
[18] F. Zhou, M. Cococcioni, C.A. Marianetti, D. Morgan, G. Ceder, Phys. Rev. B 70 (2004).
[19] C.Y. Ouyang, S.Q. Shi, M.S. Lei, J. Alloys Compd. 474 (2009) 370–374.
[20] G. Kresse, D. Joubert, Phys. Rev. B 59 (1999) 1758–1775.
[21] G. Kresse, J. Hafner, Phys. Rev. B 49 (1994) 14251–14269.
[22] G. Kresse, J. Furthmuller, Comput. Mater. Sci. 6 (1996) 15–50.
[23] G. Kresse, J. Furthmuller, Phys. Rev. B 54 (1996) 11169–11186.
[24] J.P. Perdew, K. Burke, Y. Wang, Phys. Rev. B 54 (1996) 16533–16539.
[25] M. Cococcioni, S. de Gironcoli, Phys. Rev. B 71 (2005) 16.
[26] A.I. Liechtenstein, V.I. Anisimov, J. Zaanen, Phys. Rev. B 52 (1995) R5467–R5470.
[27] T. Ohzuku, M. Kitagawa, T. Hirai, J. Electrochem. Soc. 137 (1990) 769–775.
[28] J.M. Tarascon, E. Wang, F.K. Shokoohi, W.R. Mckinnon, S. Colson, J. Electrochem. Soc. 138 (1991) 2859–2864.
[29] W. Liu, K. Kowal, G.C. Farrington, J. Electrochem. Soc. 145 (1998) 459–465.
[30] B.N. Figgis, M.A. Hitchman, Ligand Field Theory and its Applications, Wiley-VCH, New York, 2000.
[31] H.A. Jahn, E. Teller, Proc. R. Soc. Lond. A: Math. Phys. Sci. 161 (1937) 220–235.
[32] H. Hayakawa, T. Takada, H. Enoki, E. Akiba, J. Mater. Sci. Lett. 17 (1998) 811–812.
[33] A.S. Wills, N.P. Raju, J.E. Greedan, Chem. Mater. 11 (1999) 1510–1518.
[34] V. Massarotti, D. Capsoni, M. Bini, P. Scardi, M. Leoni, V. Baron, H. Berg, J. Appl. Crystallogr. 32 (1999) 1186–1189.
[35] Z.X. Wang, H. Ikuta, Y. Uchimoto, M. Wakihara, J. Electrochem. Soc. 150 (2003) A1250–A1254.
[36] J. Molenda, J. Marzec, K. Swierczek, D. Palubiak, W. Ojczyk, M. Ziemnicki, Solid State Ionics 175 (2004) 297–304.